Wind Dependencies of Deep Cycle Turbulence in the Equatorial Cold Tongues

JAMES N. MOUM,[a] WILLIAM D. SMYTH,[a] KENNETH G. HUGHES,[a] DEEPAK CHERIAN,[b] SALLY J. WARNER,[c] BERNARD BOURLÈS,[d] PETER BRANDT,[e,f] AND MARCUS DENGLER[e]

[a] *College of Earth, Ocean, and Atmospheric Sciences, Oregon State University, Corvallis, Oregon*
[b] *National Center for Atmospheric Research, Boulder, Colorado*
[c] *Departments of Physics and Environmental Studies, Brandeis University, Waltham, Massachusetts*
[d] *Institut de Recherche pour le Développement, Brest, France*
[e] *GEOMAR Helmholtz Centre for Ocean Research Kiel, Kiel, Germany*
[f] *Kiel University, Kiel, Germany*

(Manuscript received 4 October 2022, in final form 16 May 2023, accepted 18 May 2023)

ABSTRACT: Several years of moored turbulence measurements from χpods at three sites in the equatorial cold tongues of Atlantic and Pacific Oceans yield new insights into proxy estimates of turbulence that specifically target the cold tongues. They also reveal previously unknown wind dependencies of diurnally varying turbulence in the near-critical stratified shear layers beneath the mixed layer and above the core of the Equatorial Undercurrent that we have come to understand as deep cycle (DC) turbulence. Isolated by the mixed layer above, the DC layer is only indirectly linked to surface forcing. Yet, it varies diurnally in concert with daily changes in heating/cooling. Diurnal composites computed from 10-min averaged data at fixed χpod depths show that transitions from daytime to nighttime mixing regimes are increasingly delayed with weakening wind stress τ. These transitions are also delayed with respect to depth such that they follow a descent rate of roughly 6 m h^{-1}, independent of τ. We hypothesize that this wind-dependent delay is a direct result of wind-dependent diurnal warm layer deepening, which acts as the trigger to DC layer instability by bringing shear from the surface downward but at rates much slower than 6 m h^{-1}. This delay in initiation of DC layer instability contributes to a reduction in daily averaged values of turbulence dissipation. Both the absence of descending turbulence in the sheared DC layer prior to arrival of the diurnal warm layer shear and the magnitude of the subsequent descent rate after arrival are roughly predicted by laboratory experiments on entrainment in stratified shear flows.

SIGNIFICANCE STATEMENT: Only recently have long time series measurements of ocean turbulence been available anywhere. Important sites for these measurements are the equatorial cold tongues where the nature of upper-ocean turbulence differs from that in most of the world's oceans and where heat uptake from the atmosphere is concentrated. Critical to heat transported downward from the mixed layer is the diurnally varying deep cycle of turbulence below the mixed layer and above the core of the Equatorial Undercurrent. Even though this layer does not directly contact the surface, here we show the influence of the surface winds on both the magnitude of the deep cycle turbulence and the timing of its descent into the depths below.

KEYWORDS: Tropics; Atmosphere–ocean interaction; Diapycnal mixing; Diurnal effects; Mixed layer; Mixing

1. Introduction

Over most of the ocean, a turbulent mixed layer forms at night due to the combination of wind and surface cooling (Shay and Gregg 1986). Turbulence extends for some tens of meters below the surface and is isolated from deeper waters by a thin layer of stable stratification (Anis and Moum 1994). Early observations of mixing in the central equatorial Pacific showed the surprising result that, while there was a well-defined nocturnal mixed layer, diurnally varying turbulence extended into stratified waters below (Moum and Caldwell 1985; Gregg et al. 1985). This deep nocturnal turbulence was eventually termed the "deep cycle" (hereinafter DC). The combination of high turbulence diffusivity and stable stratification creates a strong flux of heat from the mixed layer into the ocean interior and thus plays an important role in the climate system (Moum et al. 2009, 2013).

These early observations (Moum et al. 1989) showed that DC turbulence depends strongly on wind stress, particularly the component that is antiparallel to the equatorial undercurrent and therefore amplifies the shear on its upper flank. More recent analyses of long-term mooring data (Smyth et al. 2021) have shown that the strength of DC turbulence is governed primarily by wind stress but also directly by the local shear. Those analyses pertained to daily-averaged measurements and therefore did not resolve the diurnal cycle. Here, we explore the dependence of diurnally cycling, deep turbulence on wind stress and on the shear of the equatorial zonal current system.

A fundamental component of the DC mechanism is the shear between the Equatorial Undercurrent (EUC), typically near 100-m depth at 140°W, and the surface South Equatorial Current. This shear works against stratification (maintained by the combination of solar heating and cold equatorial

Corresponding author: James N. Moum, jim.moum@oregonstate.edu

DOI: 10.1175/JPO-D-22-0203.1

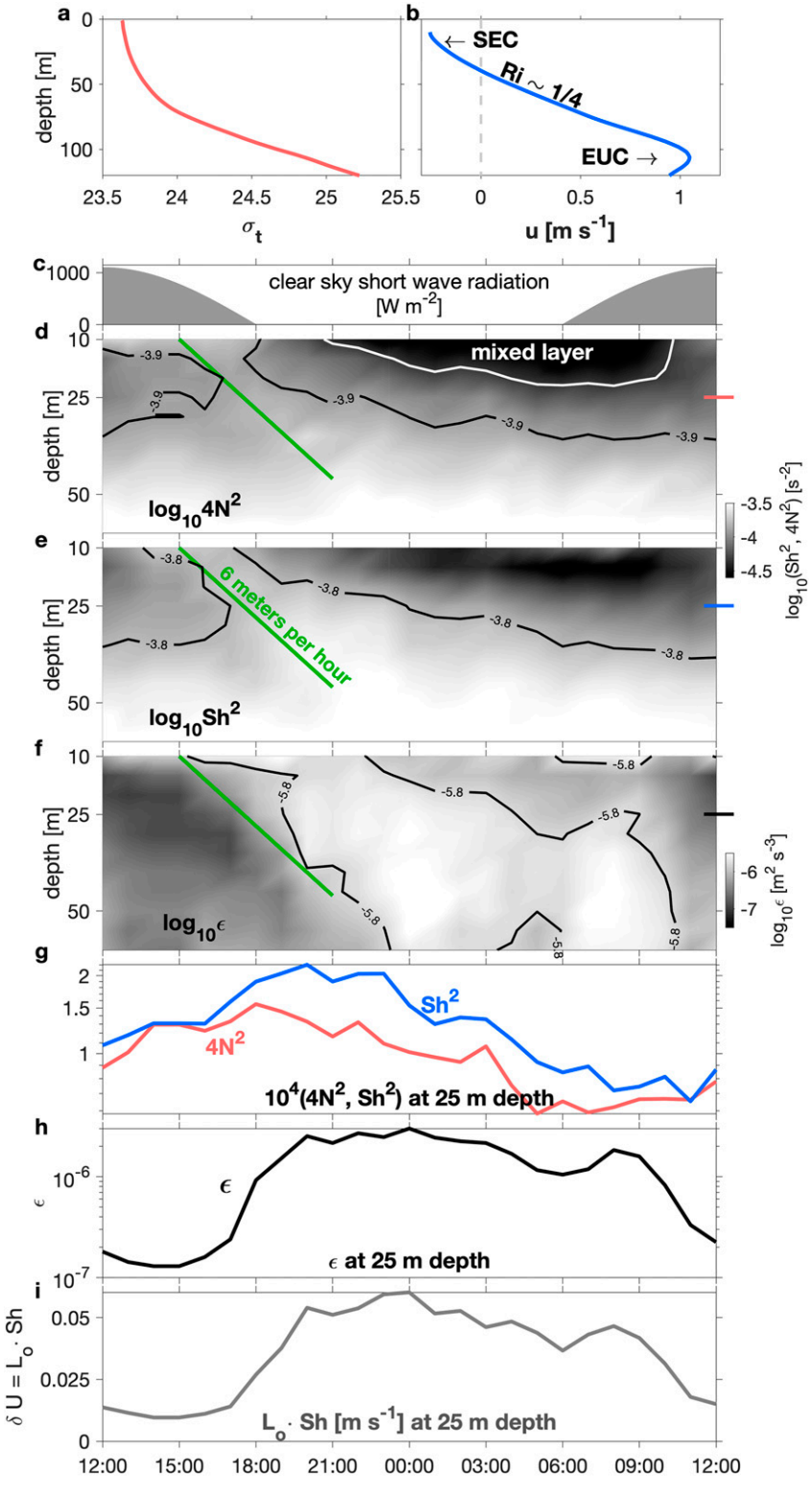

FIG. 1. Time-dependent vertical structure of DC turbulence averaged over 8 days of profiling measurements at 0°, 140°W in 2008 (Moum et al. 2009; Smyth et al. 2013): (a) Potential density σ_t. (b) Zonal velocity u shifted by -0.3 m s^{-1} to show the more typical westward-flowing South Equatorial Current (SEC) at the surface. The Equatorial Undercurrent is

upwelling) to keep the gradient Richardson number Ri near its critical value of 1/4 (Smyth 2020). This persistent state is preferentially nudged toward and beyond critical as the end of the solar day nears, presumably due to the shear-induced deepening of the base of the diurnal warm layer that forms during net daytime heating (Hughes et al. 2021), a hypothesis discussed in more detail here in section 6a.

The deepening of the stratified shear layer, followed by the initiation of DC turbulence, is depicted in the diurnal composite shown in Fig. 1, based on the 8 days of detailed profiling measurements from late 2008 examined by Smyth et al. (2013). During this period the mean depth of the EUC was about 100 m (Fig. 1b). The layer descends from near the surface to about 60 m at a rate close to 6 m h^{-1} (Figs. 1d–f). The time-lagged arrival of the layer at depth is immediately followed by large values of turbulence kinetic energy dissipation rate ϵ as indicated by the line plots in Figs. 1g and 1h from 25-m depth. Indeed, the sheared layer is found to preferentially trigger shear instability (Smyth et al. 2013). Averaged daily and over the depth range of the DC, ϵ is governed primarily by zonal wind stress (Smyth et al. 2021). The wind affects DC turbulence in two ways: by providing the energy source for the equatorial zonal current system and, on a shorter time scale, by creating the daytime surface shear layer.

Present knowledge of DC turbulence has come almost exclusively from the Pacific cold tongue at 0°, 140°W. The detailed depiction represented in Fig. 1 can only be obtained from shipboard profiling measurements. Observations using moored turbulence instruments (χpods; Moum and Nash 2009) provide longer records that show responses to a broader dynamic range of winds, tropical instability waves, ENSO, and other long time scale phenomena, albeit without the detailed vertical structure available from the shipboard measurements. We now have sufficiently long records to define the DC signal in the eastern Atlantic cold tongue, specifically at 0°, 10°W and at 0°, 23°W (Moum et al. 2022). Measurements from both regions are evaluated and compared here to more generally characterize the dependence of DC turbulence on wind and shear. The data are briefly presented in section 2. In section 3, we compare the current shear and wind stress at the three sites, using these to test a proposed proxy for ϵ. The diurnal time–depth dependence of ϵ is examined through diurnal composites at each χpod depth in section 4 and its wind dependence in section 5. These results are briefly compared with the only comparable equatorial results we know of in section 6a and observed descent rates are interpreted in relation to laboratory measurements of entrainment rates in stratified shear flows (section 6b). Conclusions follow in section 7.

2. Data

The measurements discussed here were made by χpods deployed on the equatorial moorings at 0°, 140°W, part of the TAO/TRITON array in the Pacific Ocean (McPhaden et al. 1998) and at 0°, 23°W and 0°, 10°W, part of the PIRATA array in the Atlantic Ocean (Bourlès et al. 2019). Mooring details, history, and data are found online (https://www.pmel.noaa.gov/gtmba/).

χpods have been deployed on the TAO/TRITON mooring at 0°, 140°W since September 2005 and on the PIRATA moorings at 0°, 10°W and 0°, 23°W since March 2014. Nominal χpod depths and depth ranges of both the mixed layer base and the EUC core at each location are indicated in Fig. 2.

χpods were developed to obtain long time series of turbulence measurements from which are derived estimates of relevant turbulence parameters, including ϵ, used here to quantify turbulence magnitude. Details of the measurement and analysis of the turbulence signals are found in Moum and Nash (2009), Zhang and Moum (2010), and Perlin and Moum (2012). A complete analysis primer (Warner 2020) describes the computation from the raw χpod data with speed and stratification inputs from moored temperature and velocity data.

At each mooring location is a mooring pair: a surface mooring on which is deployed temperature and conductivity sensors, frequently a current meter in the 10–20-m depth range as well as our χpods, and a separate subsurface mooring at 1-km nominal separation that houses an upward-looking 150-kHz acoustic Doppler current profiler (ADCP) at 250–300-m depth. The ADCP data are sampled with 8-m bins, averaged at hourly intervals and then gridded to 5-m bins. From these data is computed the squared current shear $\mathrm{Sh}^2 = u_z^2 + v_z^2$, where u and v are hourly values of zonal and meridional currents and the subscript z represents the vertical derivative.

To match these ADCP depth bins, we fit cubic Akima splines to combine temperature and salinity from discrete depths on the surface mooring and create a smooth vertical profile (Warner 2020), following the method described by Pham et al. (2017). From these smoothed profiles are computed the vertical temperature gradient T_z and squared buoyancy

←

indicated as EUC. The remaining panels are plotted as diurnal composites from 1200 to 1200 LT to highlight nighttime DC turbulence. (c) Clear-sky shortwave radiation to indicate solar time. Depth–time image plots of (d) $\log_{10}4N^2$, where the squared buoyancy frequency $N^2 = -g\rho_z/\rho_0$ represents density stratification, ρ is the depth-dependent density, ρ_0 is a background reference value, subscript z represents differentiation with respect to the vertical, and g is Earth's gravitational acceleration. (e) $\mathrm{Log}_{10}\mathrm{Sh}^2$, where the squared current shear $\mathrm{Sh}^2 = u_z^2 + v_z^2$ and v is the meridional component of velocity. (f) Turbulence dissipation rate $\log_{10}\epsilon$. In (d)–(f) the green line indicates a constant descent rate of 6 m h^{-1}. Composite time series at 25-m depth of (g) $4N^2$ (red), Sh^2 (blue), (h) ϵ, and (i) a velocity scale $\delta U = L_o$, with Sh defined in section 6b and the Ozmidov scale $L_o = \sqrt{\epsilon/N^3}$. The 25-m depth horizons are indicated in (d)–(f) by the colored tics on the right vertical axes.

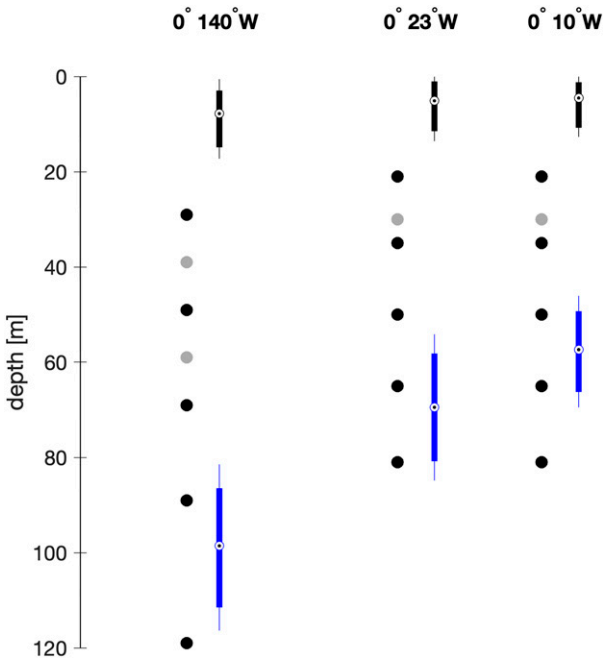

FIG. 2. χpod depths in the cold-tongue deployments at the equator and 140°, 23°, and 10°W. Primary deployment depths are indicated by the black circles. The depths indicated by the gray circles were occupied less frequently. Also indicated are the depth ranges of mixed layer base (black whiskers) and Equatorial Undercurrent core (blue whiskers). The center dots indicate median depths of hourly values, thick bars extend over the 25th–75th percentiles, and the whiskers extend to the 10th and 90th percentiles.

frequency $N^2 = -g\rho_z/\rho_0$, where g is the gravitational acceleration, ρ_z is the density gradient, and ρ_0 is a background reference value. Values of current speed and N^2 are interpolated from the gridded data to χpod depths as inputs to the computations of turbulence quantities.

The surface moorings include wind anemometers at 4-m height from which wind stress τ is estimated by correcting hourly winds to 10-m height and applying the formulation of Large and Pond (1981) as described by Warner (2020).

3. Winds, current shear, and mixing in the cold tongues

Here we contrast some basic properties relevant to DC turbulence at our three sites. Specifically, we compare mixed layer and EUC core depths, wind stress, and mean values of current shear, N^2 and ϵ between the mixed layer base and the EUC core. We then compare proposed parameterizations for DC turbulence.

a. Site comparisons

The ranges of mixed layer depths (MLD)[1] based on hourly data do not differ significantly at the three sites (Fig. 2). EUC depths (both based on hourly data) are deepest at 140°W and progressively shallower from 23° to 10°W. Because the ADCP measurements are limited to depths below 25 m at 10°W (and to below 30 m at 23° and 140°W) because of sidelobe contamination by the sea surface, the current structures above the EUC core depth at 10° and 23°W are only barely resolved.

Time series of τ based on 10-day averages at the three sites (Figs. 3a–c) show seasonal variations at 140° and 23°W with peak-to-peak amplitudes greater than 0.05 Pa. Mean values of τ at 140°W are greater than at 23°W by 20% (Table 1). The mean value of τ at 10°W is slightly smaller than that at 23°W, while the seasonal variability is considerably greater. A fundamental distinction is the dominance of zonal wind stress at 140°W and of meridional wind stress at 10°W (Table 1), a dominance that prevails throughout the year. At 23°W the wind stress varies seasonally from predominantly zonal to predominantly meridional.

Averaged values of N^2, Sh^2, and ϵ over 10 days in time were computed over the depth range roughly bounded above by the MLD and below by the EUC core (as in Fig. 2). In practice, we define this range as [27.5, 37.5] m at 10°W, [27.5, 47.5] m at 23°W, and [27.5, 75] m at 140°W. These depth ranges avoid the weakly sheared regions immediately above the EUC core and target the maximum values of Sh^2 in the DC layer. They include the uppermost three χpods at 10° and 23°W and the uppermost five χpods at 140°W. Time series of these averaged variables are shown in Fig. 3.

Time mean values of Sh^2 in the DC layer are about 3× greater at 10°W and (2× greater at 23°W than at 140°W (Table 1). At the higher values, the $4N^2$, Sh^2 data pairs representing 10° and 23°W tend below the critical value of Ri = 1/4 (Fig. 4). In contrast, the lower values of Sh^2 and N^2 at 140°W follow Ri = 1/4 reasonably well. We revisit this point in the appendix and in the discussion (section 6d), in part because it suggests a potential source of measurement uncertainty.

Values of ϵ were averaged at the χpods that cover the depth range encompassing the MLD to EUC core. Over this depth range, the time mean value at 140°W is 80% greater than at the shallower sites in the Atlantic cold tongue (Table 1). The higher values are dominated by the period prior to 2012, corresponding to the period of reduced atmospheric warming (England et al. 2014; Risbey 2015) and not sampled at the Atlantic cold-tongue sites. The 140°W record missed the significant 2017 La Niña, precluding a clean distinction between pre-2012 and post-2012 mixing. This is particularly unfortunate as it has been conjectured that excess ocean heat uptake, a measure of which χpods provide (Moum et al. 2013), during 2000–12 may be responsible for the reduced atmospheric warming and that the cold tongues take up a disproportionate amount of heat from the atmosphere (Holmes et al. 2019).

At 140°W, ϵ is significantly correlated with both $|\boldsymbol{\tau}|$ and Sh^2 (Table 2). At 23°W, ϵ is significantly correlated with $|\boldsymbol{\tau}|$ but not with Sh^2. At 10°W, ϵ is correlated with neither.

b. Dissipation proxies

Wind stress and shear contribute to three proxies for ϵ. The first derives from a production–dissipation balance of the turbulence kinetic energy equation in which the Reynolds

[1] MLD is defined from our gridded temperature profiles as the depth at which the temperature is 0.015°C less than that at 1-m depth.

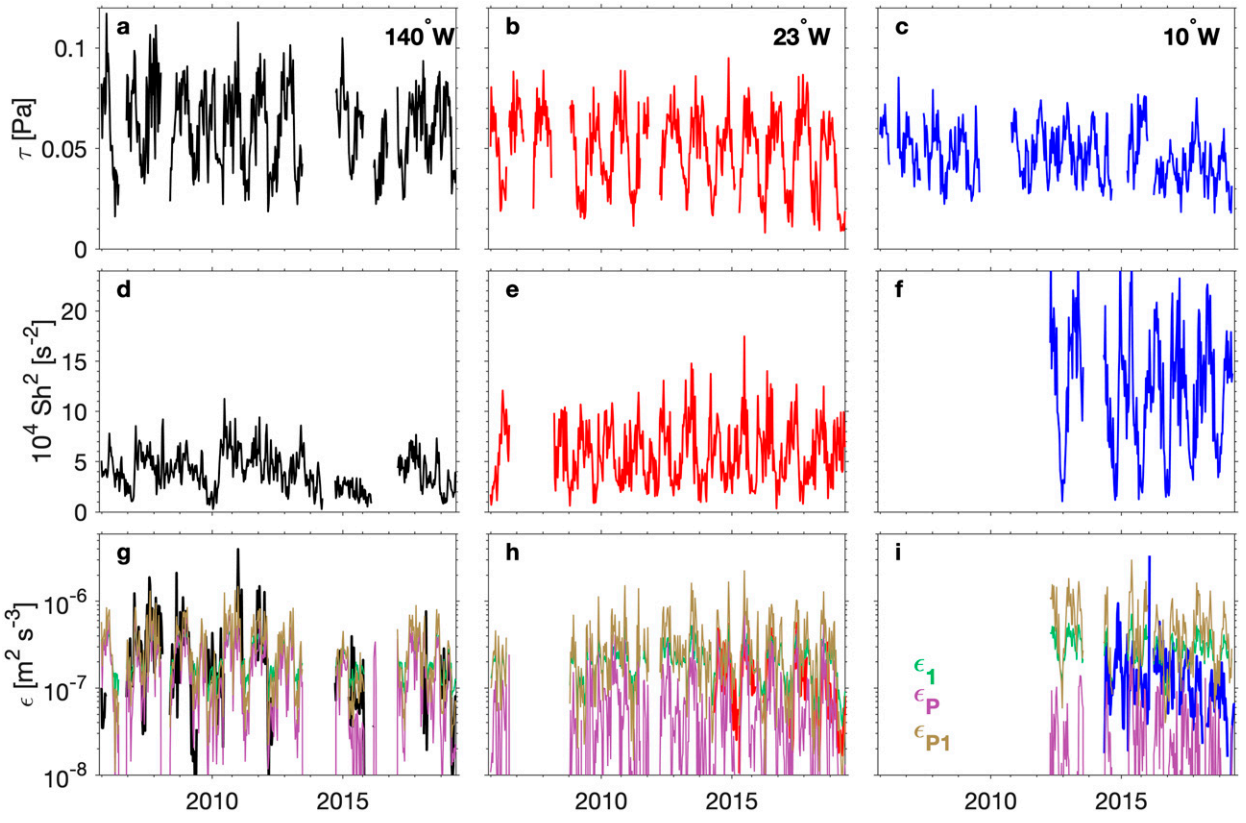

FIG. 3. Time series of (a)–(c) $|\boldsymbol{\tau}|$, (d)–(f) Sh^2, and (g)–(i) ϵ between mixed layer and EUC core depths at 140°, 23° and 10°W for the period 2005–19. These data have been averaged over 10 days. Also shown in (g)–(i) are three proxies for ϵ as described in the text.

stress is represented by the squared friction velocity in the water $u_*^2 = |\boldsymbol{\tau}|/\rho_0$ and the shear is that of the DC layer (Moum et al. 1989; Smyth et al. 2017). That is, $\epsilon_1 \propto u_*^2\mathrm{Sh}$. From the 1984 Tropic Heat experiment (Moum et al. 1989),

$$\epsilon_1 = 0.2u_*^2\mathrm{Sh}. \tag{1}$$

The constant value of 0.2 was replicated from scaled averages of χpod profiles at the three equatorial sites 140°, 23°, and 10°W by Moum et al. (2022). This parameterization is represented in Figs. 3g–i.

A second proxy was proposed by Smyth et al. (2021) based on a broad statistical analysis of factors considered to contribute to DC turbulence. This evaluation employed only the χpod data at 0°, 140°W and led to the estimate

$$\epsilon_P = (0.2\boldsymbol{\tau}\cdot\mathbf{Sh}/\rho_0)^2/J_b^{\mathrm{sw}}. \tag{2}$$

where J_b^{sw} is the solar component of the surface buoyancy flux, and negative values of the dot product $\boldsymbol{\tau}\cdot\mathbf{Sh}$ are set to zero. The coefficient value 0.2^2 (more precisely 0.0414) was calibrated by matching the long-term mean of ϵ. Variations of J_b^{sw} on 10-day time scales are $< 50\%$ (Smyth et al. 2021, their Fig. 2e) so that variations in ϵ_P are governed by variations in $\boldsymbol{\tau}\cdot\mathbf{Sh}$.

The vector form ϵ_P incorporates the wind stress $\boldsymbol{\tau}$ working in the direction of the shear vector $\mathbf{Sh}$. At 140°W in the Pacific these vectors are, for the most part, aligned (Table 1) and no values of $\boldsymbol{\tau}\cdot\mathbf{Sh}$ from 10-day averages are less than 0. This is also the location where the coefficient was defined (Smyth et al. 2021) and here ϵ_P reasonably represents observed values of ϵ as indicated in terms of mean values, as well as dynamic range and median values (Figs. 3, 5, and 6). At 10°W, where wind and shear vectors are mostly misaligned, ϵ and ϵ_P are

TABLE 1. Mean values of wind stress magnitude $|\boldsymbol{\tau}|$; zonal and meridional wind stress components τ_x and τ_y, respectively; Sh^2; and ϵ. The 95% bootstrapped confidence intervals are indicated in parentheses; Sh^2 and ϵ were averaged over the χpods between MLD and EUC core.

Location	$\lvert\boldsymbol{\tau}\rvert$ (Pa)	τ_x (Pa)	τ_y (Pa)	$10^4\mathrm{Sh}^2$ (s^{-2})	$10^7\epsilon$ ($\mathrm{m}^2\ \mathrm{s}^{-3}$)
10°W	0.046 (0.045, 0.048)	−0.017	0.032	12 (11, 13)	1.5 (1.3, 1.8)
23°W	0.050 (0.048, 0.051)	−0.037	0.026	5.8 (5.5, 6.0)	1.6 (1.4, 1.7)
140°W	0.061 (0.059, 0.063)	−0.059	0.013	4.0 (3.8, 4.2)	2.8 (2.3, 3.2)

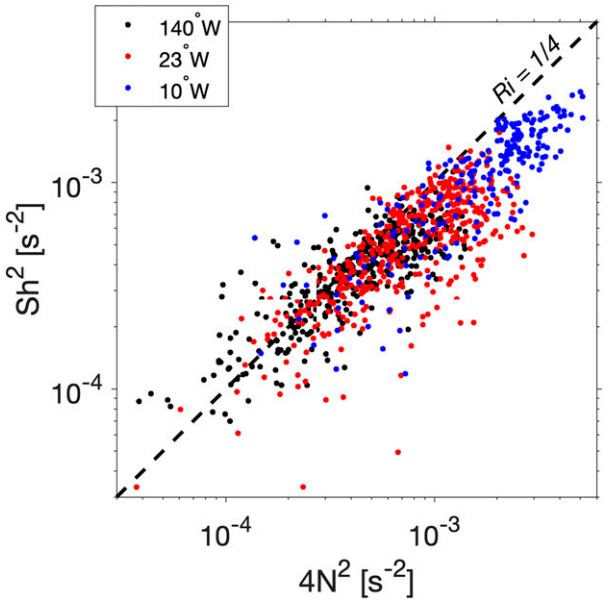

FIG. 4. Scatterplot of $4N^2$ vs Sh^2 computed as 10-day averages over the DC layer at the equator and 140°W (black), 23°W (red) and 10°W (blue).

correlated (Table 2, Fig. 5) but the magnitude of ϵ_P significantly underestimates ϵ (Figs. 3i, 5, and 6c). To a lesser extent, the value of ϵ_P at 23°W also underestimates ϵ on 10-day averages, again a consequence of vector misalignment. At 23°W, 15 (of 149) 10-day values of $\boldsymbol{\tau} \cdot \mathbf{Sh}$ are less than 0. At 10°W, 34 (of 191) 10-day values are less than 0. At all three locations, ϵ_P represents mean values of ϵ well (Moum et al. 2022), although, as Smyth et al. (2021) point out, it does not account for the observed variability.

We also consider a variant of ϵ_P without the dot product:

$$\epsilon_{P1} = \frac{(0.2|\boldsymbol{\tau}||\mathbf{Sh}|/\rho_0)^2}{J_b^{\mathrm{sw}}} = \frac{\epsilon_1^2}{J_b^{\mathrm{sw}}}. \tag{3}$$

The parameter ϵ_{P1} reasonably represents mean and median values as well as the variability in ϵ well at all three sites. A comparison of ϵ_{P1} with ϵ is included in Figs. 3g–i, 5b, and 6d–f. At 140°W, there is marginal difference between ϵ_P and ϵ_{P1}. Although, ϵ_P slightly underestimates median values of ϵ (Fig. 6a) and ϵ_{P1} slightly overestimates medians of ϵ (Fig. 6d). At 10°W, the differences are more significant, even though ϵ_P is more highly correlated with ϵ than it is with ϵ_{P1}.

TABLE 2. Correlations of DC ϵ with wind stress, squared current shear, and the proxy values ϵ_P and ϵ_{P1}. Data were averaged over 10-day periods.

Location	$\lvert\boldsymbol{\tau}\rvert$ (Pa)	Sh^2 (s^{-2})	ϵ_P ($m^2\ s^{-3}$)	ϵ_{P1} ($m^2\ s^{-3}$)
10°W	0.11	−0.02	0.36	0.12
23°W	0.63	0.15	0.72	0.71
140°W	0.54	0.44	0.66	0.66

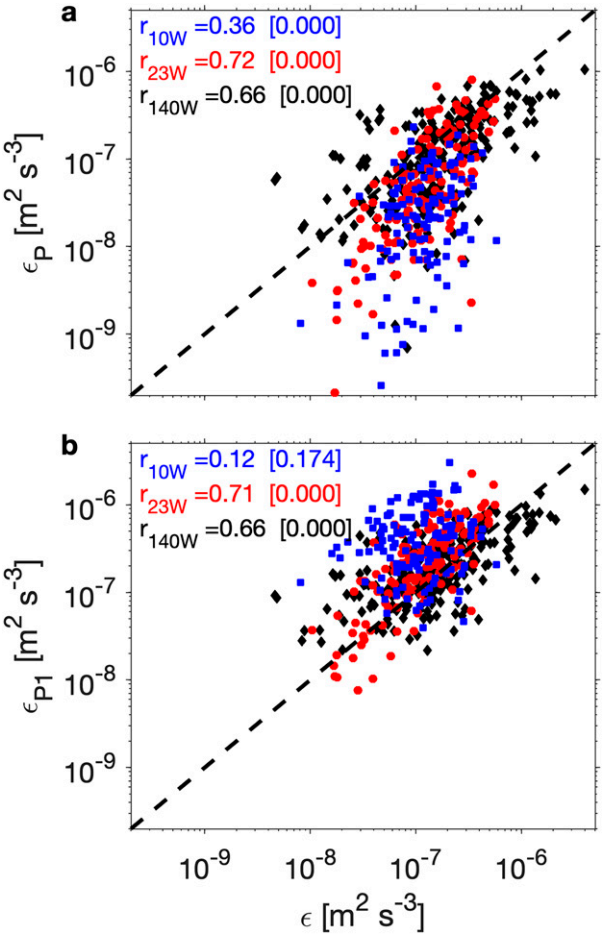

FIG. 5. Scatterplots of 10-day averaged values of (a) ϵ vs ϵ_P and (b) ϵ vs ϵ_{P1}. Correlations are Spearman, with respective p values in square brackets. The p values shown as 0.000 indicate statistical significance of the correlation.

In the derivation of ϵ_P, Smyth et al. (2021) represented the combination of wind and current shear as the dot product $\boldsymbol{\tau} \cdot \mathbf{Sh}$; but this assumption was not tested since only data from 140°W (where wind and shear are well aligned) was used. The dot product may be an oversimplification in the case of significant wind shear misalignment. For example, if wind and shear are perpendicular, the dot product is zero, but the wind could nevertheless increase Sh^2 and thus support shear instability. Misaligned winds and shear may occur during the passage of tropical instability waves along the equator (Moum et al. 2009) or by the equatorial roll, a wind-forced cross-equatorial flow (Heukamp et al. 2022).

We might therefore expect that the dot product formulation overestimates the reduction of turbulence due to wind shear misalignment, and this appears to be the case at 10°W. There, the measurements lie between ϵ_P (which overcorrects for misalignment) and ϵ_{P1} (which ignores alignment entirely).

The variables τ and Sh are clearly significant in maintaining DC turbulence. These two variables are typically not independent. In the Pacific's cold tongue, far from the eastern

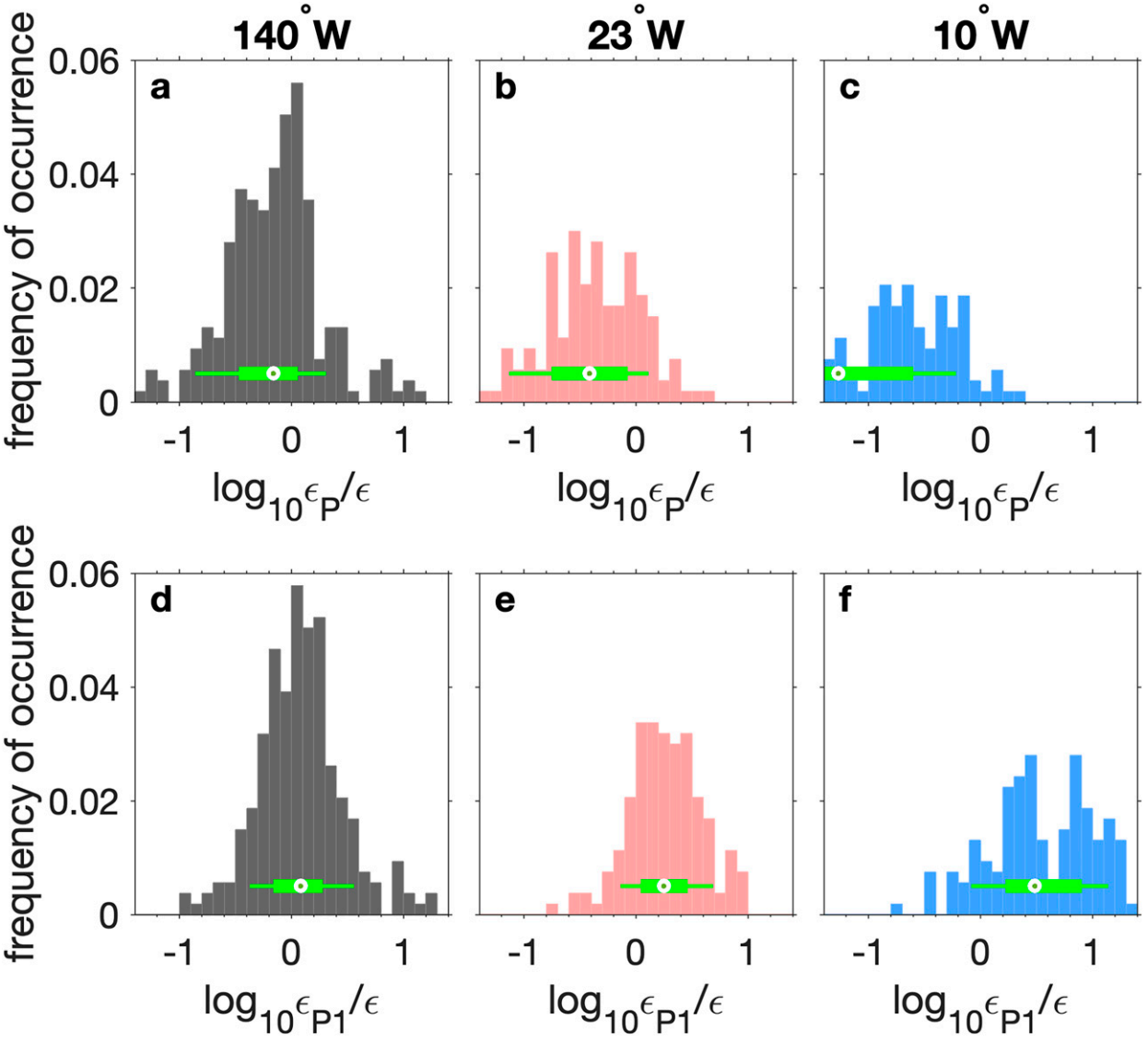

FIG. 6. Histograms of the ratios (a)–(c) ϵ_P/ϵ and (d)–(f) ϵ_{P1}/ϵ from the DC layers at the equator and (left) 140°W, (center) 23°W, and right) 10°W. Green bars indicate 80% and 50% data ranges. Dots show median values. These are the data shown in Fig. 5.

boundary, easterly trade winds drive the equatorial zonal current structure that results in the highly sheared DC layers (Philander 1981; Knox and Halpern 1982). In the eastern Atlantic, closer to the eastern boundary, the momentum balance of the EUC is more complicated particularly due to locally variable winds that substantially change in strength and direction within the seasonal cycle (Johns et al. 2014). Here, the shear in the DC layer might be additionally forced remotely via the propagation of equatorial waves (Brandt et al. 2016). However, given the presence of DC shear, there is another mechanism by which τ independently governs the nature of DC turbulence. In the next two sections, we show how decreasing wind stress retards the daily initiation of DC turbulence at the ML, thereby reducing the length of time that high values of ϵ persist in the DC layer. In addition, lower values of τ are associated with lower values of DC ϵ throughout the day.

4. Diurnal time–depth dependence of DC turbulence

Consistent diurnal variations in ϵ beneath the mixed layer that are symptomatic of DC turbulence were shown in Moum et al. (2022) as two-dimensional histograms of 10 min values of ϵ from the uppermost χpods at the three sites investigated and sorted in local time. Here and in section 5, we examine the effects that variations in wind stress have on these diurnal variations. We first generate daily composites of ϵ at all χpod depths by binning the data in 10-min bins and then computing the median value in each 10-min bin. From these daily composites we investigate the depth dependence of the DC turbulence

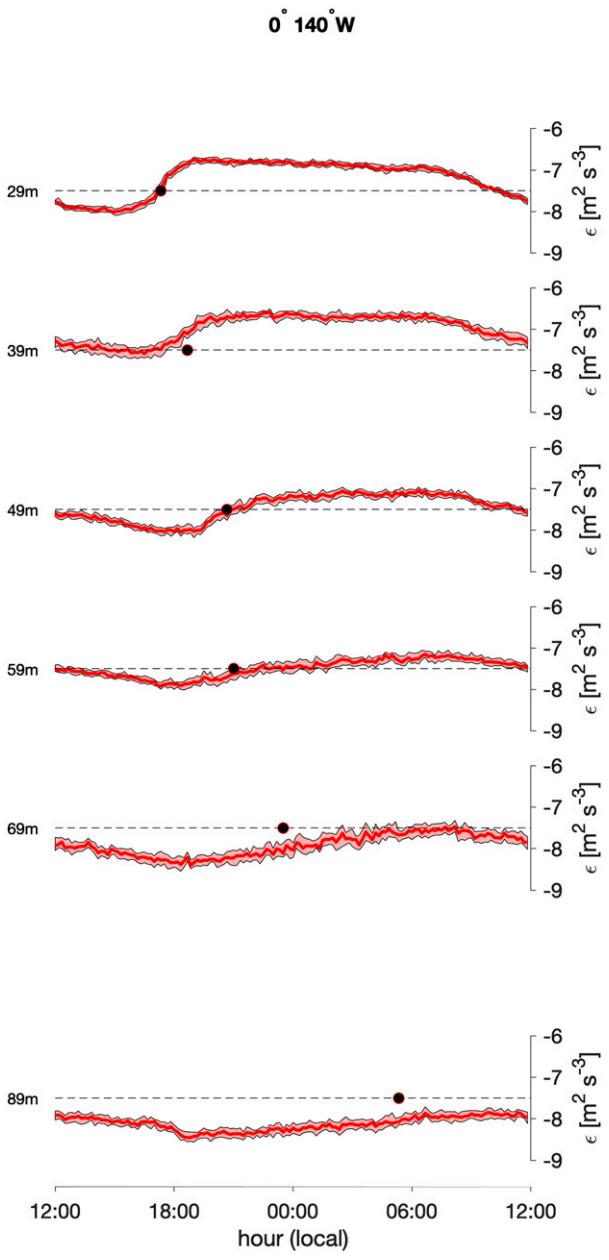

FIG. 7. Diurnal composites of ϵ from 10-min median values at the equator and 140°W from χpods in the upper 90 m of the water column for periods when $|\tau| > 0.075$ Pa. The 95% bootstrapped confidence levels of median values are indicated by the shaded red lines. Times of maximum values of ϵ_t at each depth are shown by black dots. The median lines are replicated by the red lines in the left column of Fig. 8.

via analysis of the multiple χpods at each location. Last, sorting by wind stress shows how winds affect the deepening rates of DC turbulence (section 5).

As a guide to examination of systematic diurnal variations of DC turbulence, consider first the diurnally sorted record at 140°W and $\tau > 0.075$ Pa (Fig. 7). Here we use median values of ϵ in 10-min bins as our metric. Mean values are roughly 10 × as large as medians and are dominated by relatively few values in ϵ distributions with typically high values of kurtosis, thereby obscuring the trends evident in Fig. 7. Systematic variations are clear at all χpod depths to 89 m. At all depths there is a general decrease in ϵ beginning after sunrise [0600 local time (LT)] and continuing to sunset (1800 LT). At 29-m depth, around sunset, there is rapid increase in ϵ from daytime values to a range of higher values that remains relatively steady until sunrise. The day-to-night increases in median values of ϵ are about a factor of 10 (as are mean values of ϵ; Moum et al. 2022).

At 140°W during the highest winds, peak nighttime and daytime values of ϵ are slightly larger at 39 m than at 29 m [consistent with averaged profiles of ϵ shown by Moum et al. (2022)]. Peak nighttime median values decrease with depth below 39 m. The times of minimum median values of ϵ are increasingly delayed with increasing depth. Also with increasing depth, the daytime–nighttime transition occurs over a longer period of time and that time (quantified by the maximum value of $\epsilon_t = d\epsilon/dt$ at each depth) is delayed (Fig. 7).

5. Wind dependence of DC deepening

A sorting of the data from all χpods by τ reveals a general wind dependence of the magnitudes and shapes of the diurnally varying values of ϵ and the timing of the day to night transitions (Fig. 8). The data are sorted into three ranges of τ as indicated by the figure legend. In general, wind stress increases from 10° to 23°W to 140°W in such a manner that relative sorting class sizes differ by the percentages shown in Table 3.

With decreasing wind stress, the magnitudes of nighttime values of ϵ decrease, the timing of the day–night transition is delayed, and the shape of the transition is (in most cases) flattened out (Fig. 8). While there is a clear diurnal signal at all depths above 90 m at 140°W where the median depth of the EUC core is 101 m, there is no signal below 65 m at 23°W (median EUC core depth 70 m) and below 36 m at 10°W (median EUC core depth 57 m).

We quantify the progression of the deepening of DC turbulence shown in Fig. 8 by finding the time of the maximum rate of increase of ϵ, $\epsilon_t^{\max}$, from each series after filtering each series at 1 h. The filtering is necessary to remove short time scale variability that makes determination of the daily arrival of $\epsilon_t^{\max}$ ambiguous. An example that includes 95% bootstrapped confidence limits on the median values used for the computation of $\epsilon_t^{\max}$ shows the depth-retarded timing of $\epsilon_t^{\max}$ (demonstrated in Fig. 7).

This analysis yields the deepening trajectories shown in Figs. 9a–c, at the depths where an unambiguous determination of $\epsilon_t^{\max}$ could be made. These trajectories show the arrival of DC turbulence to be progressively delayed at all depths with weakening winds.

At 140°W, arrival times of $\epsilon_t^{\max}$ at the uppermost χpod (29 m) at high, moderate, and low winds are 1730, 2100, and 2300 LT, respectively (Fig. 9; Table 4). Below this depth, DC turbulence quantified by this metric descends at the rate of roughly 6 m h^{-1}, at least in high and moderate wind states. In

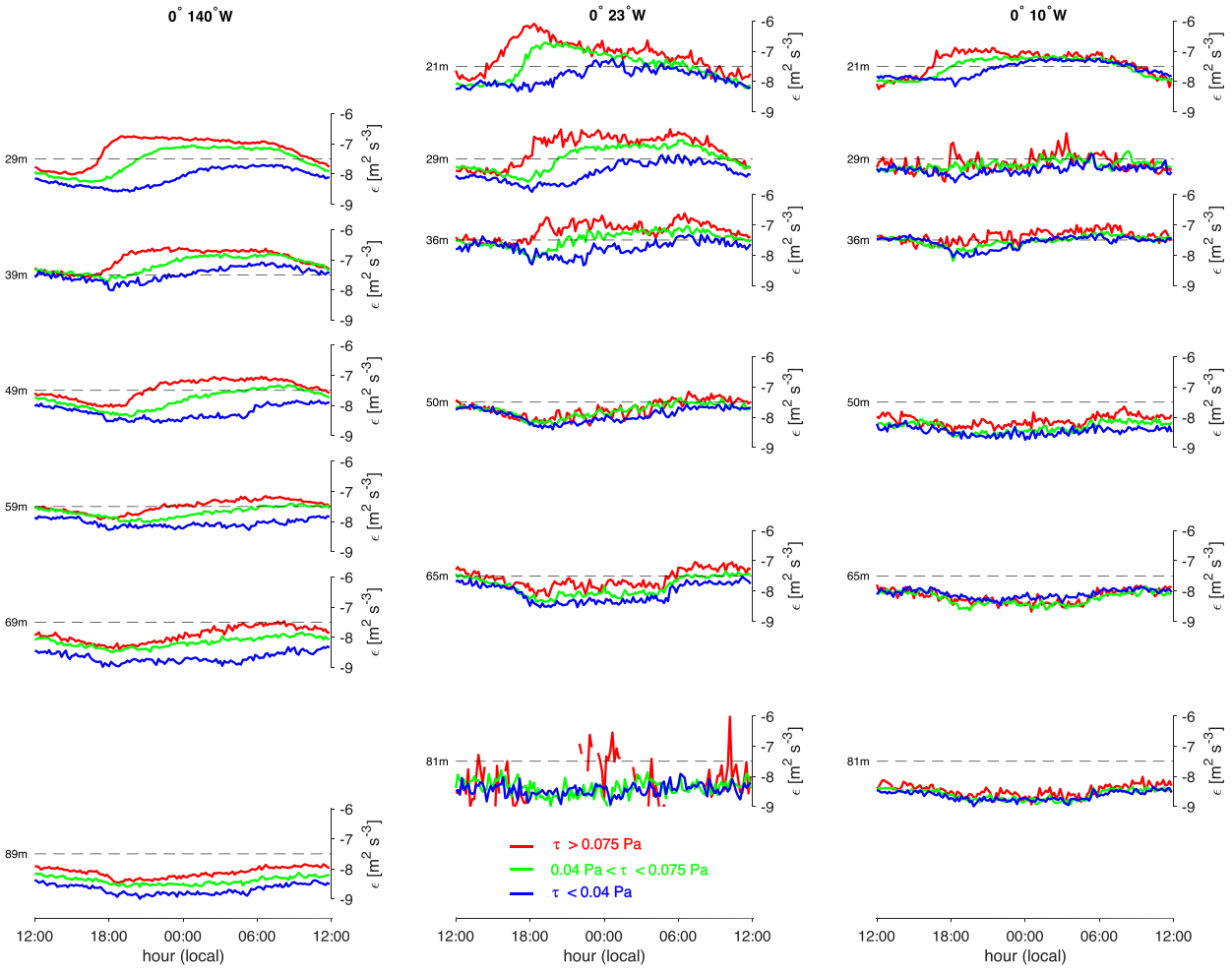

FIG. 8. Diurnal composites of ϵ at the equator and (left) 140°W, (center) 23°W, (right) 10°W from χpods in the upper 90 m of the water column. The sorting was done as described by Moum et al. (2022) and for periods when $|\boldsymbol{\tau}| > 0.075$ Pa (red), $0.04 < |\boldsymbol{\tau}| < 0.075$ Pa (green), and $|\boldsymbol{\tau}| < 0.04$ Pa (blue).

the moderate wind state, $\epsilon_t^{\max}$ is not determined from this analysis below 60 m. At the lower wind state, $\epsilon_t^{\max}$ is undefined below 29 m.

Arrival times of $\epsilon_t^{\max}$ at 30-m depth are also progressively delayed with weakening winds at 23° and 10°W and arrive at roughly the same local time as at 140°W (Table 4). Descent rates at 10° and 23°W are roughly comparable to our 6 m h^{-1} metric from 140°W (Fig. 9). Below 36 m at both 10° and 23°W the descent of the DC turbulence is undetectable.

TABLE 3. Wind stress statistics at the equator and 140°, 23°, and 10°W. Listed are percentage of times that daily averaged values of wind stress magnitude τ lies within the bounds indicated.

Location	$\lvert\boldsymbol{\tau}\rvert < 0.04$ Pa	$0.04 < \lvert\boldsymbol{\tau}\rvert < 0.075$ Pa	$\lvert\boldsymbol{\tau}\rvert > 0.075$ Pa
10°W	39%	54%	7%
23°W	35%	50%	15%
140°W	25%	46%	29%

6. Discussion

a. *Role of diurnal warm layer in delaying DC turbulence descent*

It is instructive to review independent studies at two of the sites examined here (0°, 140°W and 0°, 23°W). Detailed shipboard profiling measurements in 2008 at 0°, 140°W (Moum et al. 2009) included velocity to within 8 m of the sea surface. From a subset of these measurements Smyth et al. (2013) produced a diurnal composite that showed the descent of a highly sheared layer downward into the depth range of marginal instability between the MLD and EUC core depth (reproduced here in Fig. 1). The arrival of this layer coincided with the initiation of DC turbulence beneath the MLD as indicated by independent profiling measurements of ϵ. The diurnal composite showed the shear/mixing layer descending at a rate of roughly 6 m h^{-1}, arriving at 30-m depth at about 1800 LT.

Using data from a downward-oriented acoustic Doppler current meter deployed on the PIRATA mooring at

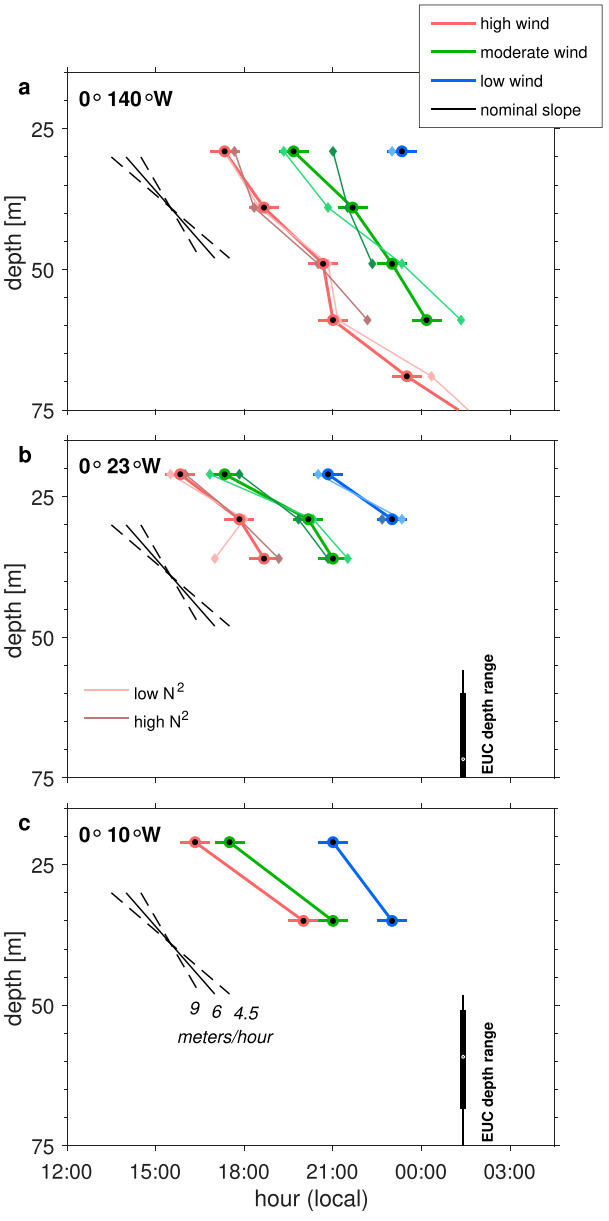

FIG. 9. Descent rates of DC turbulence at (a) 0°, 140°W; (b) 0°, 23°W; and (c) 0°, 10°W. The solid lines represent the trajectories of maximum temporal gradients of ϵ, $\epsilon_t^{\max}$, in Fig. 8. The EUC depth ranges from Fig. 2 are shown in blue. The trajectory of the red line in (a) follows the black dots in Fig. 7. For reference, a nominal descent rate of 6 m h^{-1} is indicated by the solid line. Uncertainties in timing the arrival of $\epsilon_t^{\max}$ at each depth are estimated as the filter length used to smooth the composite medians (1 h). Over a 30-m vertical span, this results in the range [4.5, 9] m h^{-1} as indicated by dashed lines, labeled in (c). Further sorting of the data by higher and lower values of N^2 are shown by the darker and lighter thin lines/symbols, respectively, and as indicated in (b).

0°, 23°W, Wenegrat and McPhaden (2015) showed a similar descending shear layer. In that case, the mixed layer arrived at 20-m depth at roughly 1800 LT (their Fig. 5e).

TABLE 4. Arrival times (local time) of $\epsilon_t^{\max}$ at 30-m depth and 0°, 140°W; 0°, 23°W; and 0°, 10°W to the nearest 0.5 h derived from Fig. 9. In the case of 0°, 10°W, the arrival times are interpolated from the detectable end points at 21 and 35 m (Fig. 9c).

Location	$\lvert\tau\rvert > 0.075$ Pa	$0.04 < \lvert\tau\rvert < 0.075$ Pa	$\lvert\tau\rvert < 0.04$ Pa
10°W	1830	2000	2200
23°W	1800	2000	2300
140°W	1730	2000	2300

In both of these cases a thin layer initially formed near the surface following the peak in stabilizing solar radiation and above a weakly sheared layer created by the previous night's convectively driven mixing. In both cases, the shear layer was stratified and Ri $\leq 1/4$ or equivalently, in the case of Wenegrat and McPhaden (2015), the reduced shear $\mathrm{Sh}^2 - 4N^2 > 0$. Note that both the Smyth et al. (2013) and Wenegrat and McPhaden (2015) results are short records with wind stress values in our *high wind* category.

These two depictions of the penetration of the shear layer from the surface into the DC layer below are roughly consistent with results discussed here. The arrival times of the shear layers and initiation of DC turbulence at depth are close to those in Table 4. In addition, descent rate estimates at all three sites range from about 4.5 to 9 m h^{-1}.

We hypothesize that the daily stratified shear layer is created near the surface by buoyancy (heat) input by the daily solar cycle and understood as the ocean's diurnal warm layer (Price et al. 1986; Sutherland et al. 2016; Moulin et al. 2018; Shcherbina et al. 2019; Hughes et al. 2020a). From upward profiling turbulence measurements in the subtropical Atlantic (26°N), Sutherland et al. (2016) showed a diurnal warm layer composite indicating a descent rate of about 2 m h^{-1}. Using measurements from a towed, surface-following platform (SurfOtter) in the tropical western Pacific for several days with varying wind stress, Hughes et al. (2020b) showed a wind dependence on the deepening of the diurnal warm layer. From ranges roughly comparable to those of wind stress in Table 3, they indicated descent rates of the diurnal warm layer of 0.3 m h^{-1} at low winds, 1 m h^{-1} at moderate winds, and up to 4 m h^{-1} at the higher wind speed. Both of these experiments were made away from the equator. In these cases, the descending diurnal warm layer ultimately mixed into the nighttime convective mixed layer driven by surface cooling.

We suspect that the wind-dependent descent of the diurnal warm layer indicated by Hughes et al. (2020b) determines the successive 2–3-h lags in arrivals of DC turbulence with successively weakening winds as indicated in Table 4. We note that projecting the 30-m arrival of the shear layer at 1800 LT (in the higher wind case) back to the surface at 6 m h^{-1} intersects the surface at 1300 LT, close to observed departures of the diurnal warm layer from the surface suggesting rapid diurnal warm layer descent at the higher wind speeds. Since the nominal descent rates are not much different from 6 m h^{-1} below the upper χpods at all wind speeds, in our scenario the delayed arrivals of the DC turbulence at lower wind speeds are consistent with slower descent rates of the diurnal warm layer shear.

b. An entrainment scaling

Perhaps we can gain some insight by considering the observed descent rate of turbulence in the DC layer with reference to laboratory studies of entrainment in stratified shear flows (Strang and Fernando 2001; Christodoulou 1986; Thorpe 1973). These studies characterize the rate of entrainment by turbulence into a layer with velocity difference δU by an entrainment velocity u_e via an entrainment coefficient $E = u_e/\delta U$ that is related to a bulk or gradient version of Richardson number, the latter of which is equivalent to our estimate Ri [Ri_g in the terminology of Strang and Fernando (2001)].

Suppose we estimate δU as the velocity difference across a turbulent overturn with length scale given by the Ozmidov scale $L_o = \sqrt{\epsilon/N^3}$ (Ozmidov 1965; Gargett 1984). This length scale represents the upper limit on turbulent overturns dictated by buoyancy suppression. In this case, $\delta U = L_o \mathrm{Sh}$ (Fig. 1i). Then

$$u_e = L_o \mathrm{Sh} E = \left(\frac{\epsilon}{N^3}\right)^{1/2} \mathrm{Sh}\, E. \tag{4}$$

As the sheared and turbulent layer deepens to 25 m in Fig. 1 the combined effects of increased Sh^2, N^2, and ϵ result in an increased $L_o\mathrm{Sh}$ from about 0.01 to more than 0.05 m s^{-1} (Fig. 1i). Before the arrival of the high values of $L_o\mathrm{Sh}$, Ri is significantly larger than 0.1. After arrival, Ri is close to 0.1. For values of $\mathrm{Ri} \leq 0.1$, E was found to be [0.02–0.04] (Christodoulou 1986), or 0.024 (Strang and Fernando 2001). For values of $\mathrm{Ri} > 0.1$, E is inversely and strongly dependent on Ri and is smaller by at least a factor of 3 (Strang and Fernando 2001, their Fig. 7). Consequently, u_e increases from significantly less than 0.5 m h^{-1} to a value in the range of 4–7 m h^{-1}. Over an 8-h interval, the lower implied descent rate would be barely noticeable. The larger rate is comparable to what we have inferred from our field measurements.

Independently, Thorpe (1973, p. 110) measured an entrainment coefficient of 0.05 ± 0.01 using a tilted tube apparatus, suggesting $u_e \sim 9$ m h^{-1} during the descent of the sheared and turbulent DC layer.

In summary, laboratory experiments on entrainment in stratified shear flows are (i) consistent with reduced descent rates of shear and turbulence in the DC layer prior to arrival of diurnal warm layer shear and (ii) comparable in magnitude to observed nighttime DC layer descent rates (or entrainment speeds) of 6 m h^{-1}. This is despite the large disparity in Reynolds numbers between ocean and laboratory. We also note mixing parameterizations that predict descent rates that are ½ (in a comparison of LES and KPP; Large and Gent 1999, their Figs. 4 and 5) and 2 times that (using LES; Pham et al. 2013, their Fig. 1) of the descent rates we have observed, although more recent LES results indicate values closer to these observations (Pham et al. 2017, their Fig. 8).

c. A day-to-day perspective from profiling experiments

The trajectories shown in Fig. 9 were defined from a total of 5800 days of data at our three sites at the depths occupied by χpods. They indicate a relatively consistent descent rate as defined by the statistics of the entirety of the data at each site. Sorted by wind stress, they show a delay in the arrival of DC turbulence with weakening winds but no difference in descent rate. The 8-day averaged diurnal composite of Fig. 1 shows with considerably more vertical detail the deepening of shear, stratification and ϵ layers that follow the green 6 m h^{-1} trajectory lines.

A more direct look at the behavior during individual days comes from shipboard profiling experiments at 0°, 140°W in 1984 (Figs. 10a,b; Moum et al. 1989), 1991 (Figs. 10c–f; Lien et al. 1995), and 2008 (Figs. 10g,h; Moum et al. 2009). Trajectories of descent rates of 6 (4.5, 9) m h^{-1} are indicated for guidance. These trajectories all pass through 30-m depth at 2000 LT, coincident with the arrival of DC turbulence at that depth during moderate winds from our χpod analysis (Table 4).

Various manifestations of the development of the DC layer appear in Fig. 10. The periods 29–30 November and 7–11 December in Fig. 10f represent moderate winds, and the appearance of DC turbulence neatly aligns with our 6 m h^{-1} trajectories intersecting 2000 LT. During periods of higher winds (i.e., 24–30 October in Fig. 10h) the DC turbulence appears earlier than the indicated trajectories. During periods of lower winds (i.e., 21 November in Fig. 10b and 6 and 12–13 November in Fig. 10d) the arrival of the DC turbulence is retarded.

The individual daily examples in Fig. 10 also show that descent rates are generally more sporadic than suggested by Fig. 9. For example, DC turbulence descends at a rate close to 3 m h^{-1} on 21 November in Fig. 10b and close to 12 m h^{-1} on 1 December in Fig. 10f. Occurrences of bursts of energetic turbulence in the DC layer (Smyth et al. 2017) separated by periods of weak turbulence are common and not very consistent with a cleanly delineated transition to DC turbulence.

d. Uncertainty

The analysis in the appendix targets several uncertainties that apply to the proxies ϵ_P and ϵ_{P1}. These are

(i) application of proxies based on 1-day-averaged data to 10-day averages,
(ii) measurement of Sh^2 in the DC layer from moored ADCPs, and
(iii) our estimation of N^2 by gridding relatively sparse measurements of T and S to 5-m vertical spacing.

We address potential uncertainty in our results relative to each of these in turn.

We have used 10-day averages in section 3 because wind stress variations are dominated by time scales of more than several days (indicated by frequency spectra in Farrar and Durland 2012). Our comparisons in Fig. A1 suggests that random variability is certainly reduced in 10-day averages of $4N^2$, Sh^2 data pairs but there is no significant bias between 1-day (too short to include significant wind stress variability) and 10-day averages.

Our comparison of Sh^2 is derived from ADCP measurements at hourly intervals from the TAO mooring at 0°, 140°W (as described in section 2) and nearby shipboard profiling with greater fidelity in both depth and time. This comparison

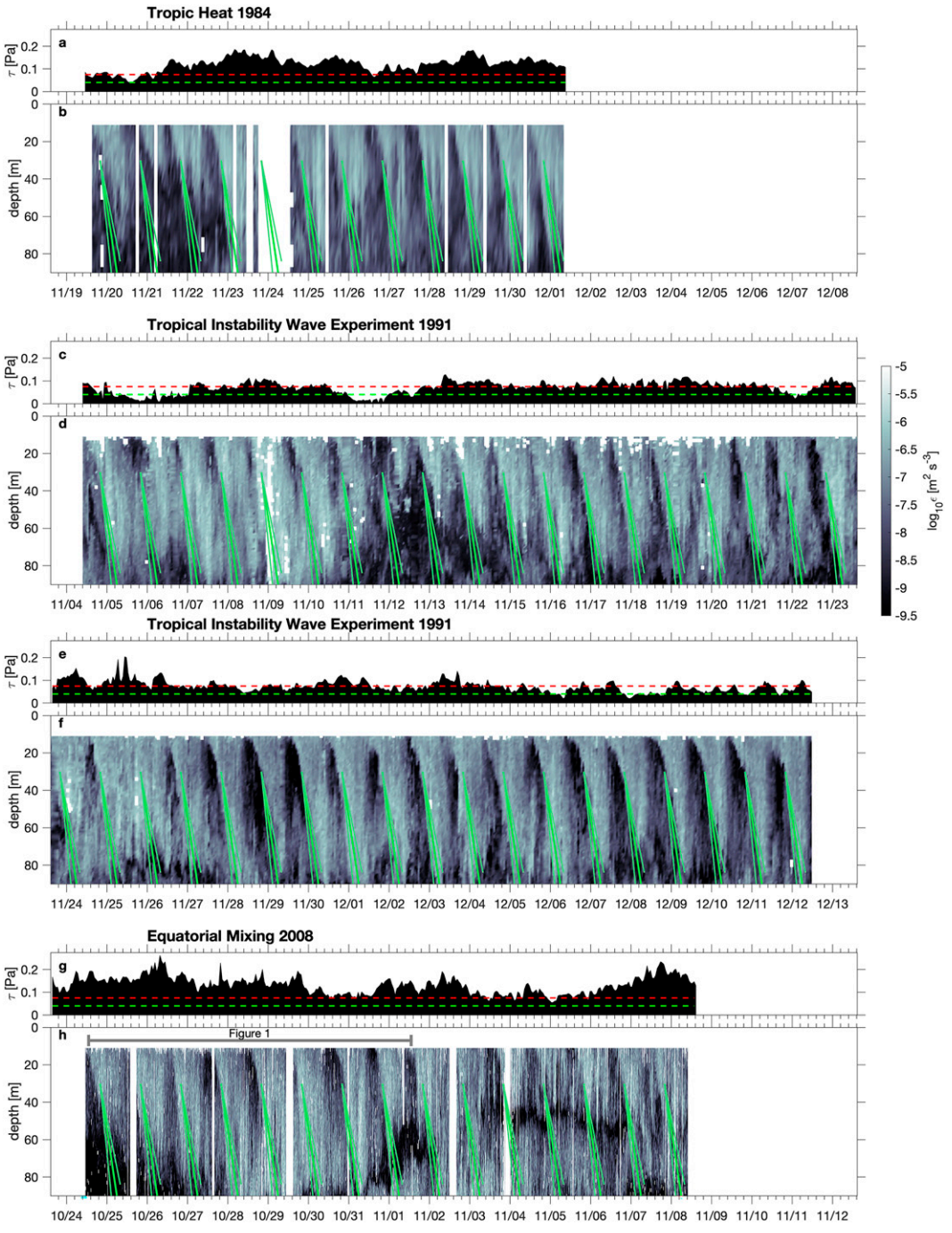

FIG. 10. (a),(c),(e),(g) Time series of wind stress and (b),(d),(f),(h) time–depth series of ϵ from three turbulence profiling experiments at 0°, 140°W in 1984, 1991, and 2008. Times are UTC. All ϵ measurements were made using shear probes on Chameleon. The horizontal red ($\tau = 0.075$ Pa) and green ($\tau = 0.04$ Pa) dashed lines in (a), (c), (e), and (g) indicate the limits used to sort χpod data. The green lines in ϵ image plots indicate descent rates of 4.5, 6, and 9 m h^{-1} and intersect 30-m depth at 2000 UTC. The data for the averaged diurnal composite shown in Fig. 1 represent the period indicated by the horizontal gray bar in (h).

indicates no bias in moored measurements of Sh^2 averaged over 30–80 m, roughly the DC layer, at 140°W (Fig. A1b).

The stratification estimated from the same coincident and collocated data over the 30–80-m depth range reveals that our estimate of N^2 obtained by gridding relatively sparse measurements on the TAO mooring underestimates that from detailed in situ profiler measurements by about 30% in terms of both mean and median values (Fig. A1c).

The absence of bias in Sh^2 is reassuring as it does not contribute to bias in our estimates of ϵ_P and ϵ_{P1}, at least at 140°W. The notion that the shallower and thinner DC layers at 10° and 23°W may be subject to a low bias in Sh^2 (based on Fig. A1) would indicate that the highest values there (Fig. 3) are yet higher. In turn, this also applies to the high values of ϵ_{P1} at these two sites (Fig. 5). This suggests at least a reappraisal of the coefficients determined by Smyth et al. (2021) based solely on data from 140°W.

Since N^2 does not appear in ϵ_P and ϵ_{P1} they are not directly affected. However, if the low bias in N^2 we have found at 140°W applies also to 10°W and/or 23°W, then an additional adjustment to increase Sh^2 is necessary so that $4N^2$, Sh^2 data pairs align with Ri = 1/4. At this stage of our understanding, there is not really a reason to expect that these data should align with Ri = 1/4, and the flows may have fundamental differences. More complete and detailed measurements in the Atlantic cold tongue are in order.

7. Conclusions

We have examined several years of moored turbulence records from our three sites in the equatorial cold tongues of Atlantic and Pacific Oceans. These records yield new insights into proxy estimates for the DC turbulence that is, so far as we know, unique to the cold tongues. They also reveal previously unknown wind dependencies that govern the timing and structure of the DC turbulence. Significant commonalities exist between the three sites despite considerable differences in magnitudes and variability of winds, current shear and turbulence (Table 1, Figs. 3 and 5). Deployment mean values of ϵ are nearly identical at 30-m depth at all sites (Moum et al. 2022). At the uppermost χpods, the ensemble of measurements clearly shows the diurnal signals symptomatic of DC turbulence (Fig. 8). There are roughly factors of 10 differences between day/night mean and median values of ϵ at these upper χpods at all three sites (Moum et al. 2022).

Transitions from daytime to nighttime mixing regimes are strongly dependent on τ (Fig. 8). In particular, (i) at all depths, ϵ increases with increasing τ, and (ii) day/night mixing transitions are delayed with decreasing τ, presumably due to the slowed descent rate of the diurnal warm layer with decreasing τ (Hughes et al. 2020b). DC turbulence descends at rates of approximately 6 m h^{-1}, independent of τ (Fig. 9), and faster than previously observed descent rates of the diurnal warm layer.

Variations in τ and DC layer Sh^2 are clearly linked to variations in the magnitude of ϵ in the DC layer, as suggested by the correlative link to ϵ_P, a matter recently investigated using large eddy simulations and data from shipboard profiling measurements in 1991 (Whitt et al. 2022, who compared directly with buoyancy flux rather than ϵ). At least in the Pacific, τ and DC layer Sh^2 are not independent, since wind stress accelerates the DC layer current shear as part of the positive Bjerknes feedback (Bjerknes 1969). But this occurs on time scales longer than diurnal. In the Atlantic, longer than diurnal time scale variations in shear seem to be more closely linked to a seasonal wave response associated with resonant basin modes. Such a resonance that is forced by the basinwide wind stress field results in an upward and downward movement of the DC layer with shallowest EUC core in boreal spring and deepest EUC core in boreal autumn (Brandt et al. 2016). At the diurnal time scale, the progressively retarded deepening at progressively lower values of τ contributes to lower values of DC ϵ not only because DC values of ϵ are smaller at low winds but also because DC turbulence is initiated later in the day and persists for a shorter period of time, thereby reducing mean values.

The prediction of the descent rate of the DC layer into already turbulent fluid below is based on laboratory experiments intended to represent the deepening of the surface mixed layer. In these experiments, a mixed layer descends by entrainment of dense fluid below (thereby increasing mixed layer density), descending into nonturbulent fluid. Despite the differences in conditions between laboratory and field experiments as well as the different scaling employed herein to arrive at our estimate of u_e, the result is quantitative agreement. In turn, this points to an improved understanding of the physics of DC layer turbulence.

Certainly, further study is needed to modify proxy estimates of ϵ for general use in regions of significant wind vector–shear vector misalignment. Also, perhaps there is a need for more intensive and detailed studies in the Atlantic Ocean's cold tongue to evaluate potential and fundamental differences in the nature of the instabilities leading to DC turbulence there in comparison with what we have learned from detailed shipboard measurements in the Pacific Ocean's.

Acknowledgments. The measurements described were funded by the National Science Foundation (Grants 1256620, 1431518, and 2048631). The participation of author W. D. Smyth was funded by NSF Grant OCE-1851520. We acknowledge the efforts of M. Neeley-Brown, R. Kreth, A. Perlin, M. Borgerson, C. Van Appledorn, P. Vutukur, J. Logan, and K. Latham in building, testing, and calibrating χpods. We are grateful for the helpful comments of Emily Shroyer on an early draft, for the assistance of NOAA's National Data Buoy Center who deploy and recover instruments on the TAO/TRITON array, and to NOAA's Pacific Marine Environmental Laboratory who coordinate shipments including our χpods to IRD (France) for deployment and recovery of the instruments on the PIRATA array. Authors P. Brandt and M. Dengler acknowledge support from the EU H2020 program (Grants 817578 TRIATLAS and 101003470 NextGEMS). The National Center for Atmospheric Research is sponsored by the National Science Foundation.

Data availability statement. All moored data, including χpod data, are available at NOAA's Global Tropical Moored Buoy Array (https://www.pmel.noaa.gov/gtmba/).

APPENDIX

Potential Limitations of Moored Estimates of N^2 and Sh^2

Our comparisons of $4N^2$ and Sh^2 in Fig. 4 suggest fundamental differences in the nature of the conditions affecting

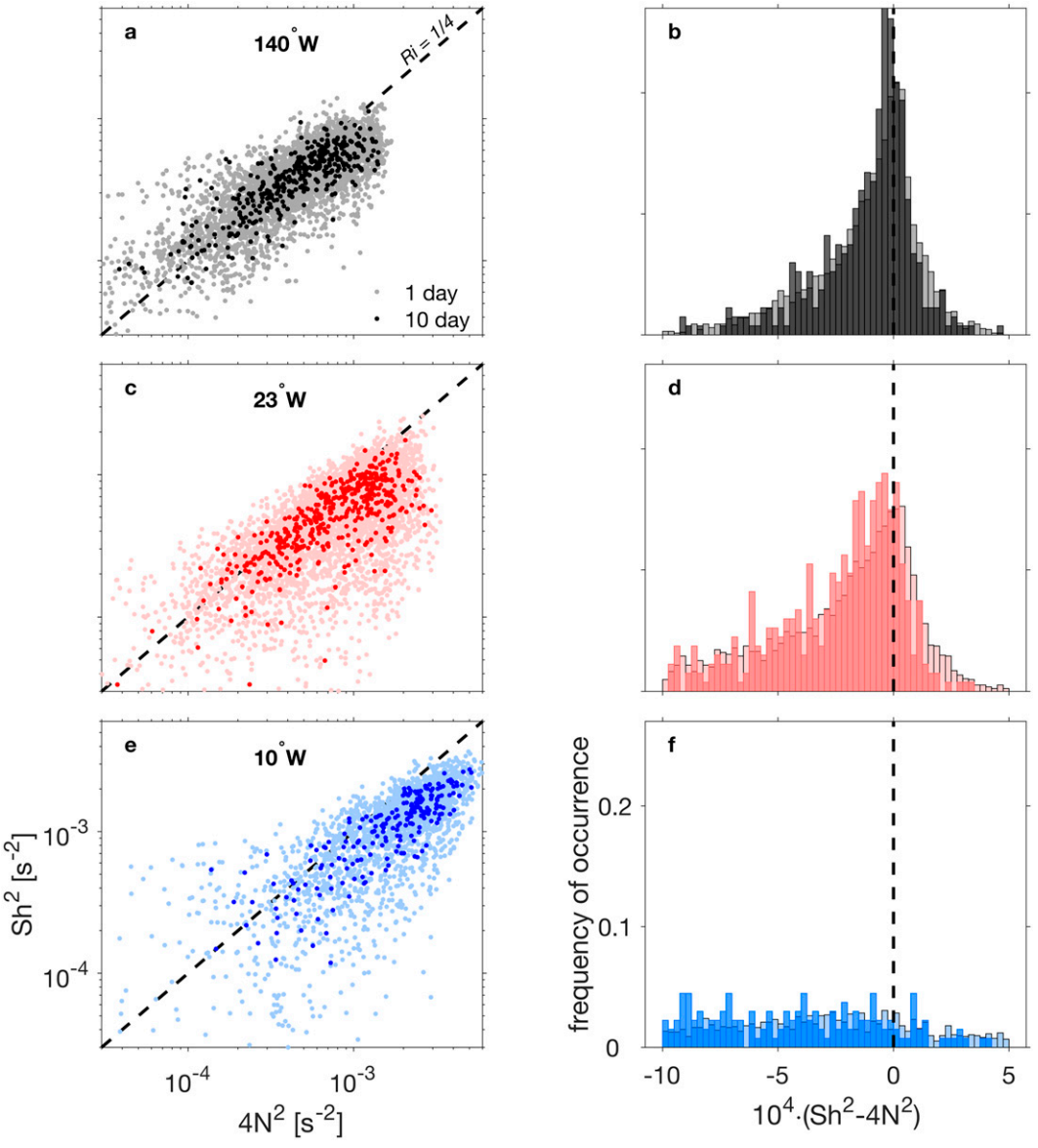

FIG. A1. Comparison of moored estimates of 1 and 10-day averages of DC layer values of $4N^2$ and Sh^2 at the equator and (a) 140°W, (c) 23°W, and (e) 10°W. (b),(d),(f) Histograms of reduced squared shear, $Sh^2 - 4N^2$. Daily averages are shown as the lighter colors on all panels.

stability (relative to Ri) between Atlantic and Pacific equatorial DC layers. In terms of our parameterizations ϵ_P and ϵ_{P1}, we might be concerned that moored estimates of Sh^2 might be biased low, at least at 10° and 23°W. An additional concern is that Smyth et al. (2021) applied ϵ_P to daily averages of τ and Sh^2 whereas we have used 10 days as our basis with the justification that wind stress variations are dominated by at least many-day time scales (Farrar and Durland 2012). Here we look more closely at the nature of the relationship between $4N^2$ and Sh^2 at our three sites and attempt to address these concerns.

In Fig. A1, we isolate the $4N^2$ and Sh^2 comparisons at the three sites and compare daily and 10-day averages. At 140°W $4N^2$, Sh^2 data pairs roughly scatter about the critical value of Ri = 1/4, and 10-day averages cluster more closely to the Ri = 1/4 line (Figs. A1a,b). Measurements from 23° and 10°W tend toward larger values of both Sh^2 and N^2. At both Atlantic sites, data pairs fall below the Ri = 1/4 metric, indicating a greater tendency for stable flow conditions, more so at 10°W. In detail, data pairs at 140°W with values $<10^{-3}$ s^{-2} also appear to tend below the Ri = 1/4 line (Fig. A1a). Distributions of reduced squared shear $Sh^2 - 4N^2$ at the three sites (Figs. A1b,d,f) emphasize the main distinction.

Is it possible that our processing of the moored data (see section 2) produces biases in Sh^2 or N^2? We address this by comparing data from the 0°, 140°W TAO mooring with

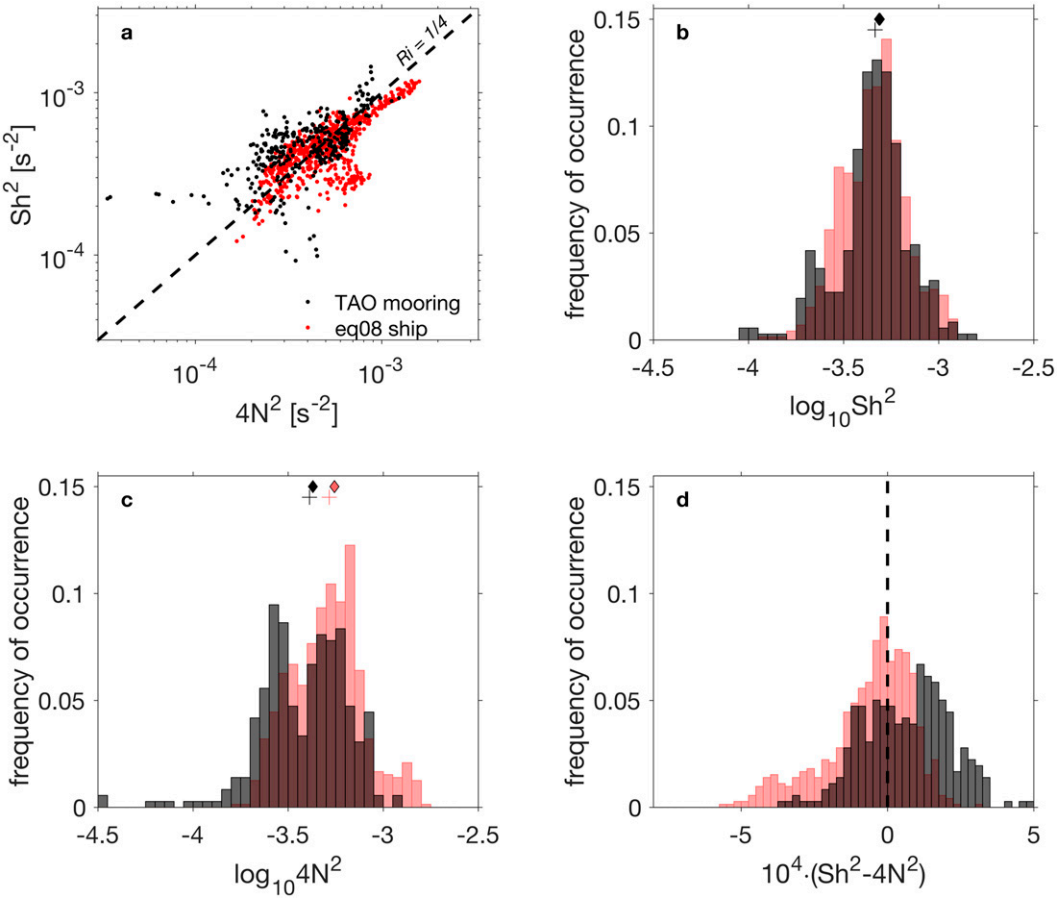

FIG. A2. Comparison of hourly-averaged estimates of $4N^2$ and Sh^2 computed over the depth interval 30–80 m at 0°, 140°W during the period of a shipboard experiment 14 Oct–08 Nov 2008: (a) $4N^2$ vs Sh^2. TAO estimates from 150-kHz ADCP on the nearby subsurface mooring are shown in black. Shipboard measurements in red were made using a hull-mounted 300-kHz ADCP at 2-m range bins. Initial 5-s averages were then averaged to 1 h for comparison. Red values of N^2 were computed from Chameleon profiles at profiling rates of 8–10 profiles per hour. (b) Histograms of Sh^2 from TAO (black) and ship (red). (c) Histograms of $4N^2$. (d) Histograms of reduced squared shear $Sh^2 - 4N^2$. In (b) and (c), diamonds represent mean values and crosses median values. The apparent absence of a red diamond/cross in (b) indicates that both mean and median values of moored and ship measurements of Sh^2 are nearly identical.

detailed shipboard measurements over 15 days in October/November 2008 (Moum et al. 2009). These datasets are separated laterally by 1–9 km as the ship maintained a position nearby the TAO mooring while profiling from the stern. The shipboard data consist of high-resolution profiling of temperature and salinity to determine N^2 and a 300-kHz hull-mounted ADCP sampled at 2-m range bins and 5-s multi-ping averages, further averaged to 1 h for comparison. We directly compare Sh^2 and $4N^2$ at hourly intervals over the depth range 30–80 m (Fig. A2). We do not believe that these data should agree on a 1–1 basis and compare them on a statistical basis. Mean and median values of Sh^2 are identical to the extent that symbols denoting these values in Fig. A2b are indistinguishable. However, mean and median values of $4N^2$ obtained from detailed profiling are greater by 30% than those obtained from the relatively sparsely instrumented mooring (Fig. A2c). This bias in N^2 tends to move the scatterplot of the TAO mooring data above the Ri = 1/4 line in Fig. A2a and to the right in Fig. A2d. Equivalently, in both cases this suggests a greater tendency toward instability.

We have greater confidence in the shipboard profiling measurements and conclude from Fig. A2 that our analysis of the data on the TAO surface mooring yields an underestimate of N^2.

REFERENCES

Anis, A., and J. N. Moum, 1994: Prescriptions for heat flux and entrainment rate in the upper ocean during convection. *J. Phys. Oceanogr.*, **24**, 2142–2155, https://doi.org/10.1175/1520-0485(1994)024<2142:PFHFAE>2.0.CO;2.

Bjerknes, J., 1969: Atmospheric teleconnections from the equatorial Pacific. *Mon. Wea. Rev.*, **97**, 163–172, https://doi.org/10.1175/1520-0493(1969)097<0163:ATFTEP>2.3.CO;2.

Bourlès, B. M., and Coauthors, 2019: PIRATA: A sustained observing system for tropical Atlantic climate research and

forecasting. *Earth Space Sci.*, **6**, 577–616, https://doi.org/10.1029/2018EA000428.

Brandt, P., M. Claus, R. J. Greatbatch, R. Kopte, J. M. Toole, W. E. Johns, and C. W. Boning, 2016: Annual and semiannual cycle of Atlantic circulation associated with basin-mode resonsance. *J. Phys. Oceanogr.*, **46**, 3011–3029, https://doi.org/10.1175/JPO-D-15-0248.1.

Christodoulou, G. C., 1986: Interfacial mixing in stratified flows. *J. Hydraul. Res.*, **24**, 77–92, https://doi.org/10.1080/00221688609499323.

England, M. H., and Coauthors, 2014: Recent intensification of wind-driven circulation in the Pacific and the ongoing warming hiatus. *Nat. Climate Change*, **4**, 222–227, https://doi.org/10.1038/nclimate2106.

Farrar, J. T., and T. S. Durland, 2012: Wavenumber-frequency spectra of inertia-gravity and mixed Rossby–gravity waves in the equatorial Pacific Ocean. *J. Phys. Oceanogr.*, **42**, 1859–1881, https://doi.org/10.1175/JPO-D-11-0235.1.

Gargett, A. E., 1984: Vertical eddy diffusivity in the ocean interior. *J. Mar. Res.*, **42**, 359–393, https://doi.org/10.1357/002224084788502756.

Gregg, M. C., H. Peters, J. C. Wesson, N. S. Oakey, and T. J. Shay, 1985: Intensive measurements of turbulence and shear in the equatorial undercurrent. *Nature*, **318**, 140–144, https://doi.org/10.1038/318140a0.

Heukamp, F. O., P. Brandt, M. Dengler, F. P. Tuchen, M. J. McPhaden, and J. N. Moum, 2022: Tropical instability waves and wind-forced cross-equatorial flow in the central Atlantic Ocean. *Geophys. Res. Lett.*, **49**, e2022GL099325, https://doi.org/10.1029/2022GL099325.

Holmes, R. M., J. D. Zika, and M. H. England, 2019: Diathermal heat transport in a global ocean model. *J. Phys. Oceanogr.*, **49**, 141–161, https://doi.org/10.1175/JPO-D-18-0098.1.

Hughes, K. G., J. N. Moum, and E. L. Shroyer, 2020a: Evolution of the velocity structure in the diurnal warm layer. *J. Phys. Oceanogr.*, **50**, 615–631, https://doi.org/10.1175/JPO-D-19-0207.1.

——, ——, and ——, 2020b: Heat transport through diurnal warm layers. *J. Phys. Oceanogr.*, **50**, 2885–2905, https://doi.org/10.1175/JPO-D-20-0079.1.

——, ——, ——, and W. D. Smyth, 2021: Stratified shear instabilities in diurnal warm layers. *J. Phys. Oceanogr.*, **51**, 2583–2598, https://doi.org/10.1175/JPO-D-20-0300.1.

Johns, W. E., P. Brandt, B. Bourlès, A. Tantet, A. Papapostolou, and A. Houk, 2014: Zonal structure and seasonal variability of the Atlantic equatorial undercurrent. *Climate Dyn.*, **43**, 3047–3069, https://doi.org/10.1007/s00382-014-2136-2.

Knox, R. A., and D. Halpern, 1982: Long range Kelvin wave propagation of transport variations in Pacific Ocean equatorial currents. *J. Mar. Res.*, **40**, 329–339.

Large, W. G., and S. Pond, 1981: Open ocean momentum flux measurements in moderate to strong winds. *J. Phys. Oceanogr.*, **11**, 324–336, https://doi.org/10.1175/1520-0485(1981)011<0324:OOMFMI>2.0.CO;2.

——, and P. R. Gent, 1999: Validation of vertical mixing in an equatorial ocean model using large eddy simulations and observations. *J. Phys. Oceanogr.*, **29**, 449–464, https://doi.org/10.1175/1520-0485(1999)029<0449:VOVMIA>2.0.CO;2.

Lien, R. C., D. R. Caldwell, M. C. Gregg, and J. N. Moum, 1995: Turbulence variability in the central Pacific at the beginning of the 1991–1993 El Nino. *J. Geophys. Res.*, **100**, 6881–6898, https://doi.org/10.1029/94JC03312.

McPhaden, M., and Coauthors, 1998: The tropical ocean-global atmosphere observing system: A decade of progress. *J. Geophys. Res.*, **103**, 14 169–14 240, https://doi.org/10.1029/97JC02906.

Moulin, A. J., J. N. Moum, and E. L. Shroyer, 2018: Evolution of turbulence in the diurnal warm layer. *J. Phys. Oceanogr.*, **48**, 383–396, https://doi.org/10.1175/JPO-D-17-0170.1.

Moum, J. N., and D. R. Caldwell, 1985: Local influences on shear flow turbulence in the equatorial ocean. *Science*, **230**, 315–316, https://doi.org/10.1126/science.230.4723.315.

——, and J. D. Nash, 2009: Mixing measurements on an equatorial ocean mooring. *J. Atmos. Oceanic Technol.*, **26**, 317–336, https://doi.org/10.1175/2008JTECHO617.1.

——, D. R. Caldwell, and C. A. Paulson, 1989: Mixing in the equatorial surface layer and thermocline. *J. Geophys. Res.*, **94**, 2005–2022, https://doi.org/10.1029/JC094iC02p02005.

——, R.-C. Lien, A. Perlin, J. D. Nash, M. C. Gregg, and P. J. Wiles, 2009: Sea surface cooling at the equator by subsurface mixing in tropical instability waves. *Nat. Geosci.*, **2**, 761–765, https://doi.org/10.1038/ngeo657.

——, A. Perlin, J. D. Nash, and M. J. McPhaden, 2013: Seasonal sea surface cooling in the equatorial Pacific cold tongue controlled by ocean mixing. *Nature*, **500**, 64–67, https://doi.org/10.1038/nature12363.

——, and Coauthors, 2022: Deep cycle turbulence in Atlantic and Pacific cold tongues. *Geophys. Res. Lett.*, **49**, e2021GL097345, https://doi.org/10.1029/2021GL097345.

Ozmidov, R. V., 1965: On the turbulent exchange in a stably stratified ocean. *Izv. Acad. Sci. USSR, Atmos. Oceanic Phys.*, **1**, 853–860.

Perlin, A., and J. N. Moum, 2012: Comparison of thermal variance dissipation rates from moored and profiling instruments at the equator. *J. Atmos. Oceanic Technol.*, **29**, 1347–1362, https://doi.org/10.1175/JTECH-D-12-00019.1.

Pham, H. T., S. Sarkar, and K. B. Winters, 2013: Large-eddy simulation of deep-cycle turbulence in an equatorial undercurrent model. *J. Phys. Oceanogr.*, **43**, 2490–2502, https://doi.org/10.1175/JPO-D-13-016.1.

——, W. D. Smyth, S. Sarkar, and J. N. Moum, 2017: Seasonality of deep cycle turbulence in the eastern equatorial Pacific. *J. Phys. Oceanogr.*, **47**, 2189–2209, https://doi.org/10.1175/JPO-D-17-0008.1.

Philander, S. G. H., 1981: The response of equatorial oceans to a relaxation of the trade winds. *J. Phys. Oceanogr.*, **11**, 176–189, https://doi.org/10.1175/1520-0485(1981)011<0176:TROEOT>2.0.CO;2.

Price, J. F., R. A. Weller, and R. Pinkel, 1986: Diurnal cycling: Observations and models of the upper ocean response to diurnal heating, cooling, and wind mixing. *J. Geophys. Res.*, **91**, 8411–8427, https://doi.org/10.1029/JC091iC07p08411.

Risbey, J., 2015: Free and forced climate variations. *Nature*, **517**, 562–563, https://doi.org/10.1038/517562a.

Shay, T. J., and M. C. Gregg, 1986: Convectively driven turbulent mixing in the upper ocean. *J. Phys. Oceanogr.*, **16**, 1777–1798, https://doi.org/10.1175/1520-0485(1986)016<1777:CDTMIT>2.0.CO;2.

Shcherbina, A. Y., E. A. D'Asaro, and R. R. Harcourt, 2019: Rain and sun create slippery layers in eastern Pacific fresh pool. *Oceanography*, **32**, 98–107, https://doi.org/10.5670/oceanog.2019.217.

Smyth, W. D., 2020: Marginal instability and the efficiency of ocean mixing. *J. Phys. Oceanogr.*, **50**, 2141–2150, https://doi.org/10.1175/JPO-D-20-0083.1.

——, J. N. Moum, L. Li, and S. A. Thorpe, 2013: Diurnal shear instability, the descent of the surface shear layer and the deep cycle of equatorial turbulence. *J. Phys. Oceanogr.*, **43**, 2432–2455, https://doi.org/10.1175/JPO-D-13-089.1.

——, H. T. Pham, J. N. Moum, and S. Sarkar, 2017: Pulsating stratified turbulence in the upper equatorial oceans. *J. Fluid Mech.*, **822**, 327–341, https://doi.org/10.1017/jfm.2017.283.

——, S. J. Warner, J. N. Moum, H. T. Pham, and S. Sarkar, 2021: What controls the deep cycle? Proxies for equatorial turbulence. *J. Phys. Oceanogr.*, **51**, 2291–2302, https://doi.org/10.1175/JPO-D-20-0236.1.

Strang, E. J., and H. J. S. Fernando, 2001: Entrainment and mixing in stratified shear flows. *J. Fluid Mech.*, **428**, 349–386, https://doi.org/10.1017/S0022112000002706.

Sutherland, G., L. Marié, G. Reverdin, K. H. Christensen, G. Broström, and B. Ward, 2016: Enhanced turbulence associated with the diurnal jet in the ocean surface boundary layer. *J. Phys. Oceanogr.*, **46**, 3051–3067, https://doi.org/10.1175/JPO-D-15-0172.1.

Thorpe, S. A., 1973: Experiments on instability and turbulence in a stratified shear flow. *J. Fluid Mech.*, **61**, 731–751, https://doi.org/10.1017/S0022112073000911.

Warner, S. J., 2020: χpod and GusT processing manual. Oregon State University, 120 pp., https://ir.library.oregonstate.edu/concern/technical_reports/r207tw79j.

Wenegrat, J. O., and M. J. McPhaden, 2015: Dynamics of the surface layer diurnal cycle in the equatorial Atlantic Ocean (0°, 23°W). *J. Geophys. Res. Oceans*, **120**, 563–581, https://doi.org/10.1002/2014JC010504.

Whitt, D. B., D. A. Cherian, R. M. Holmes, S. D. Bachman, R.-C. Lien, W. G. Large, and J. N. Moum, 2022: Simulation and scaling of the turbulent vertical heat transport and deep-cycle turbulence across the equatorial Pacific cold tongue. *J. Phys. Oceanogr.*, **52**, 981–1014, https://doi.org/10.1175/JPO-D-21-0153.1.

Zhang, Y., and J. N. Moum, 2010: Inertial-convective subrange estimates of thermal variance dissipation rate from moored temperature measurements. *J. Atmos. Oceanic Technol.*, **27**, 1950–1959, https://doi.org/10.1175/2010JTECHO746.1.